Applied Energy 414 (2026) 127808

Contents lists available at ScienceDirect

Applied Energy

journal homepage: www.elsevier.com/locate/apen

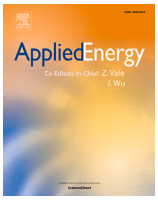

A novel engineering wake model for helix-actuated wind turbine wakes

Tim Dammann [a,*], Daan van der Hoek [a], Wei Yu [b], Jan-Willem van Wingerden [a]

[a] Delft Center for Systems and Control, Faculty of Mechanical Engineering, Mekelweg 2, 2628 CD Delft, Zuid-Holland, Netherlands
[b] Wind Energy Section, Department of Flow Physics and Technology, Faculty of Aerospace Engineering, Kluyverweg 1, 2629 HS Delft, Zuid-Holland, Netherlands

HIGHLIGHTS

- Developed a novel velocity deficit and additional turbulence intensity model for wind turbines operating under Helix control.
- The model showed high agreement with test data across a range of ambient and operational conditions.
- Applied the model to an offshore wind farm to showcase the benefits of wind farm control at a farm level.

ARTICLE INFO

Keywords:
Wind turbine wakes
Active wake control
Wake modelling
Wind farm control
Wind farm power prediction
Helix

ABSTRACT

Engineering wake models are essential tools in wind farm design and operation. Their computational efficiency enables rapid layout optimization, energy calculation, and turbine control setpoint design. As wind farms grow in scale and density, wake interactions between turbines limit overall energy capture and increase structural loading. Wind Farm Control strategies have become critical for mitigating these effects. While wake steering, the intentional yaw misalignment of upstream turbines, has consistently demonstrated power gains, new dynamic control strategies are emerging. Among these, the Helix approach has shown particular promise in accelerating wake recovery and improving downstream power production. While engineering models for wake steering are well established, dedicated models for the Helix approach remain unavailable. This study presents a novel steady-state engineering model for predicting the velocity deficit and added turbulence of wind turbines operating under Helix actuation. The proposed model extends double-Gaussian velocity deficit and bell-curve– shaped turbulence intensity formulations to account for Helix-specific effects of actuation amplitude and ambient turbulence. Calibration and validation against high-fidelity large-eddy simulations demonstrate strong agreement across a wide range of operating conditions. The model accurately reproduces wake recovery trends, variations in the velocity-deficit profile, turbulence distributions, and the resulting downstream power availability. Finally, a case study on a large offshore wind farm illustrates that, under typical offshore atmospheric conditions, Helix control and wake steering yield individual power gains of up to 2.5% and 6.1%, respectively, while their combined application achieves total power gains of up to 7.1%.

1. Introduction

Engineering wake models, often termed ‘analytical’ or ‘low-fidelity’ models, are foundational tools for the design and operation of wind farms. Their computational efficiency allows for fast estimation of aerodynamic interactions, specifically the velocity deficits and added turbulence intensity (TI) arising from turbine wakes. This capability is essential for critical industry applications, including the optimization of wind farm layouts [1], the calculation of annual energy production (AEP), and the design of wind farm control setpoints [2]. The increasing demand for renewable energy continues to drive the development of larger and more densely packed wind farms. In such configurations, aerodynamic wake interactions are amplified, leading to substantial power losses and increased structural loading on downstream machines [3]. Effective Wind Farm Control (WFC) strategies are therefore necessary to mitigate these detrimental effects, by coordinating the operation of individual turbines to achieve a global plant-level objective, such as power maximization or load mitigation [4].

WFC strategies can be broadly classified as static or dynamic. Static approaches involve a fixed operational offset from the baseline control scheme. Static induction control, for instance, reduces the thrust of upstream turbines (down-regulation) to decrease wake intensity with the

* Corresponding author.
Email address: t.dammann@tudelft.nl (T. Dammann).

https://doi.org/10.1016/j.apenergy.2026.127808
Received 17 November 2025; Received in revised form 9 February 2026; Accepted 27 March 2026
Available online 3 April 2026

initial goal of increasing farm power [5,6]. However, several studies have shown that static induction control is not effective for power maximization [7–9], which is why the research focus has shifted towards wake steering control. Here, the upstream turbine is intentionally misaligned with the incoming wind. This yaw misalignment deflects the wake, steering it away from downstream turbines to increase the overall power capture of the array. Wake steering has thus far been extensively studied experimentally [10,11], in simulations [12,13], and in field experiments [3,14] with consistently promising results.

In contrast, dynamic strategies employ time-varying control inputs, a notable example being dynamic induction control (DIC), which periodically changes the turbine's thrust via sinusoidal variations of the collective blade pitch. The goal is to promote turbulent mixing, thereby re-energizing the wake for downstream power gains [15]. However, DIC has been shown to induce significant alternating forces on the rotor, raising concerns about its detrimental impact on turbine structural lifetime [16]. Among emerging dynamic techniques, the Helix approach stands out as a promising alternative. This strategy employs dynamic individual pitch control to re-energize the wake while aiming to mitigate the load and power fluctuations associated with DIC [16]. The Helix mechanism involves imposing periodic out-of-phase variations in individual blade pitch angles to exert a rotating force on the flow. The direction (clockwise or counter-clockwise) of this force, determined by the pitch actuation's phase offset, results in a forced helical meandering of the wake. This induced motion enhances turbulent mixing with the ambient flow, leading to a faster wake recovery and, consequently, increased power capture by downstream turbines. Several studies involving Large Eddy Simulations (LES) and wind tunnel experiments have confirmed these benefits, showing significant increases in downstream power production [16–18]. While the Helix approach has been shown to enhance power production, recent studies indicate that it can also lead to increased turbine loads, primarily associated with higher pitch amplitudes [19]. Exploring this balance, LES studies have shown that power gains increase with Helix amplitudes up to a six-degree threshold, beyond which the impact on structural loads becomes too large [20]. In multi-turbine arrays, optimizing power output depends on the Helix phase offset between turbines [17], a principle later used to develop a controller that utilizes this offset to further increase array power capture [21].

As WFC strategies mature towards commercial application, the development of engineering models capable of predicting their specific aerodynamic effects becomes imperative. Standard engineering models, whose formulations typically depend on the turbine's thrust coefficient (C_T), are intrinsically capable of simulating static induction control. Significant research efforts have been dedicated to extending these models to capture the wake deflection physics of wake steering [22,23]. In contrast, there remains a notable lack of engineering models capable of accurately reproducing the complex, time-averaged flow phenomena induced by dynamic control strategies such as the Helix approach.

To establish such a model, we first revisit the theoretical foundations on which it must be built. Engineering wake modelling for conventional baseline operation has a long and well-documented history. The earliest engineering model is the top-hat model proposed by Jensen [24], which assumes a uniform velocity deficit within a linearly expanding wake. This concept was later refined through momentum-conserving formulations, such as those of Frandsen et al. [25]. More recently, a new generation of models has emerged to describe the spatial distribution of the velocity deficit, exemplified by the single-Gaussian model of Bastankhah and Porté-Agel [26]. Derived from the conservation of mass and momentum, it posits a self-similar Gaussian profile for the velocity deficit, which fits well in the far-wake region. However, the single-Gaussian profile fails to capture the complex flow physics in the near-wake region, particularly the double-peaked velocity deficit profile induced by the pressure drop and root/tip vortices.

The limitations of single-Gaussian wake profiles motivated the development of double-Gaussian wake models [27–29]. By superimposing two Gaussian functions, these models can more accurately represent the characteristic velocity deficit shape in the near wake, transitioning smoothly to a single-Gaussian profile further downstream. A recent advancement was presented by Qian and Ishihara [30], which introduced an enhanced double-Gaussian formulation with improved parameterizations. Their approach incorporates thrust and turbulence-dependent tuning parameters, leading to greater accuracy across a wider range of atmospheric stability conditions. However, their model, like its predecessors, is formulated for turbines operating under conventional baseline control.

Initial efforts to model Helix-induced wakes include the active wake mixing model implemented in the National Renewable Energy Laboratory's (NREL) FLOw Redirection and Induction in Steady State (FLORIS) framework [31], as well as an early comparative study evaluating the effectiveness of Helix control and wake steering in wind farms [32]. Although these models provide reasonable approximations, they were developed by tuning the parameters of existing baseline wake models. As a result, these models fail to capture the complex, time-averaged flow structures and additional turbulence effects characteristic of Helix-induced wakes.

The main contributions of this paper are threefold. First, we introduce a novel steady-state engineering wake model specifically developed for Helix control. Building upon the double-Gaussian framework to better represent variations in the velocity deficit profile, the proposed model incorporates the effects of time-averaged, forced helical meandering on wake recovery. Its formulation explicitly accounts for the dependence of the time-averaged velocity deficit on both the Helix control amplitude and the ambient TI. Second, we propose an initial model to predict the increase in wake-added turbulence induced by Helix control. This model captures amplitude-dependent changes in added TI, which are subsequently superimposed on the ambient TI. Both models are formulated and calibrated using high-fidelity LES training data and validated against independent LES test cases covering a range of Helix amplitudes and ambient turbulence conditions. The resulting models provide a computationally efficient framework capable of accurately predicting power output and enabling rapid optimization of Helix-based wind farm control strategies. Third, we present a case study applying the proposed models to an offshore wind farm in the North Sea to demonstrate the benefits of Helix control, wake steering, and their combined application for enhancing farm-level power production.

The remainder of this paper is structured as follows. Section 2 describes the high-fidelity simulation framework used for model development and validation. Section 3 presents the analytical derivation of both the model for the velocity deficit and the added turbulence intensity. Section 4 shows how the model was tuned and validated using the test data. In Section 5, we apply both models to a reference offshore wind farm and analyze the resulting effects on the farm's power output. Lastly, Section 6 discusses the conclusions and insights gained from this study.

2. High fidelity simulation setup and dataset generation

The LES-solver used for all simulations is AMR-Wind [33], an adaptive-mesh incompressible flow solver developed for wind energy applications. The solver is built upon the AMReX library for block-structured adaptive mesh refinement [34]. It solves the spatially filtered, incompressible Navier–Stokes equations on a Cartesian grid that can be locally refined by combining the finite volume and finite-difference methods. For temporal discretization, a second-order accurate Crank-Nicolson scheme was used. Consistent with high-fidelity practices for AMR-Wind [35], the advection terms were discretized using the fifth-order accurate WENO-Z scheme [36]. AMR-Wind allows for an internal coupling with OpenFAST [37], which was used in this study.

For all simulations, the IEA 22-MW reference wind turbine [38] was used, which has a rotor diameter of $D = 284\,\mathrm{m}$ and a rated wind speed of $11\,\mathrm{ms}^{-1}$. The computational domain, shown in Fig. 1(a), was designed

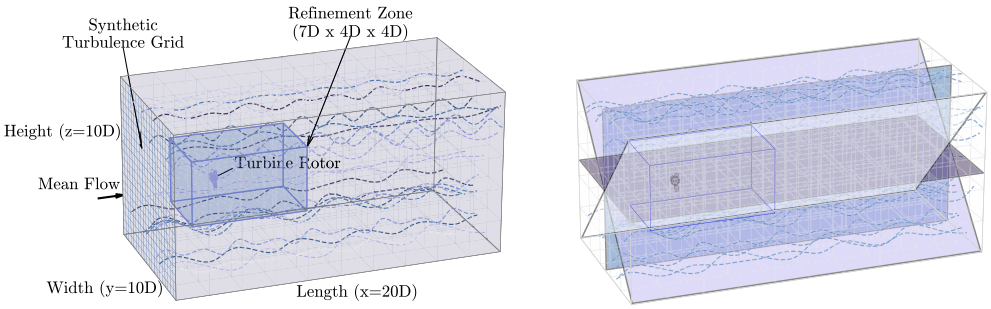

(a) LES domain (b) Sampling planes

Fig. 1. Visualization of the simulation domain (a) and sampling planes (b) in AMR-Wind. The length of the domain is 20 D in the streamwise direction and 10 D in both lateral directions. The turbine rotor is positioned at a distance of 4 D from the inlet.

to isolate the turbine wake dynamics from any atmospheric effects, in close resemblance to [17]. The domain extends $L_x = 20\,D$ in streamwise direction and $L_{y,z} = 10\,D$ in the lateral and vertical directions. The turbine was placed in the lateral and vertical center at a distance of 4 D from the inlet boundary.

The domain was discretized using a base grid of isotropic 10 m cells. A single level of mesh refinement was applied, sharing its centroid with the turbine rotor. The refinement region extended from 2 D upstream to 5 D downstream of the rotor and spanned 4 D in both lateral directions, resulting in a grid resolution of $\Delta x = 5\,\text{m}$ in the refined zone and approximately 56 cells per D. A constant time step of $\Delta t = 0.05\,\text{s}$ was used, satisfying the actuator line Courant Friedrichs Lewy condition of $\frac{u_{tip}\Delta t}{\Delta x} < 1$, given a rotor speed of $\Omega = 5\,\text{rpm}$ for the chosen mean wind speed of $8\,\text{ms}^{-1}$. The mean wind speed of $8\,\text{ms}^{-1}$ was selected, corresponding to operation in Region II where the turbine achieves its maximum thrust coefficient ($C_{T,\text{max}}$), thus generating the strongest wake deficit effects and thereby motivating the use of wake mixing techniques. The total runtime of each simulation was 2700 s, of which the first 700 s (corresponding to approximately one flow-through time) was discarded to exclude transient effects.

A mass inflow condition was prescribed at the inlet boundary and a pressure outflow condition was applied at the outlet boundary. To prevent atmospheric boundary layer interaction and focus solely on the wake evolution, slip-wall boundary conditions were applied to all lateral domain boundaries. The effects of the tower, ground, and gravity were neglected. A uniform inflow was set, coming from 270° (westward, in meteorological convention) with a constant mean wind speed per case. The incoming wind was superimposed with body forces, derived from a synthetic turbulence grid. Each grid was generated, using the TurbSim [39] software. Turbulence fields were generated by concatenating turbulence time series of six different seeds using the IEC Kaimal Spectrum. To achieve a shear-free inflow, the mean shear profile was subtracted from the generated turbulence fields. To capture subgrid-scale effects, the Smagorinsky turbulence model was used with a constant Smagorinsky coefficient of $C_s = 0.135$.

Within the LES domain, the wind turbine was modelled using the Actuator Line Model (ALM). The ALM approach resolves the aerodynamic forces along each blade, allowing for the direct implementation of the periodic, out-of-phase individual pitch commands that constitute the Helix control strategy. The turbine rotor was modelled as a flexible body, using the Elastodyn module in OpenFAST with a 4° precone and no shaft tilt. The Gaussian smearing of the actuator point forces was chosen as $\epsilon = 10$, leading to an epsilon by grid (EBG) ratio of $\epsilon/\Delta_x = 2$. Based on prior observations of the authors, the number of actuator points was set to 59 (equal to the number of defined airfoil sections), since any other number caused non-smooth velocity profiles in the near-wake [40]. The dynamic individual pitching motion, allowing the helical wake deflection, was implemented, using the Reference Open Source Controller (ROSCO) [41], developed by the NREL, which was coupled to OpenFAST. The Helix actuation was simulated in a counter-clockwise manner and the actuation frequency was kept at an optimal value referring to a Strouhal number of $S_t = 0.28$ as this value results in the maximal downstream power gains [42].

Velocity was sampled through four planes (a horizontal hub slice, a vertical hub slice, and two diagonal hub slices), as illustrated in Fig. 1(b). Each plane consisted of (280×560) sampling probes (10 m spacing). After sampling, the planes were spatially averaged to obtain an axisymmetric representation of the flow field, which was then temporally averaged.

A total of 22 LES cases are investigated in order to derive the analytical formulations in Section 3 and examine the influence of TI and Helix actuation amplitude on the time-averaged velocity and turbulence fields, exerted by the turbine. Each case took approximately 50,000 CPU hours. All cases are listed in Table 1. The 22 simulated cases were divided into a training dataset (16 cases) and a testing dataset (6 cases). The testing set was composed of cases 1, 2, 4, 6, 9, and 17.

3. Helix engineering wake model formulation

The focus of this work lies in accurately modelling the influence of actuation amplitude and increased TI on the time-averaged velocity field of a Helix wake. The model for the mean velocity deficit extends the double-Gaussian approach of Qian and Ishihara [30], while the model for added TI extends the formulation by Frandsen [43], incorporating Helix-specific parameterizations. Both models implicitly account for the loss in thrust force in relation to actuation amplitude, which is modelled using an amplitude-dependent third-order polynomial fit.

3.1. Full wake characteristics

Fig. 2 presents the time-averaged axisymmetric streamwise velocity field for baseline operation and Helix actuation for low and high turbulence cases. The difference becomes particularly evident in the low turbulence case. Helix actuation causes significant contraction of the wake core, while the continuous helical deflection of the wake induces a jet of higher-velocity air along the centerline in the far wake. Under high turbulence conditions, this jet vanishes as enhanced turbulent mixing dissipates the coherent structures in the far wake. The wake core, however, remains noticeably shortened.

Fig. 3(a) shows the mean streamwise velocity profiles obtained after slicing the velocity field data at distinctive downstream distances. The morphology of this profile exhibits a strong dependence on the actuation amplitude, which accelerates the transition from the double-Gaussian profile in the near-wake to a single-Gaussian distribution in the mid wake. This evolution progresses towards a more uniform, flat-Gaussian shape in the mid wake region. Further downstream, in the far wake,

Table 1
List of LES cases. The thrust coefficient throughout all simulations was kept constant at a value of $c_t = 0.87$ (disregarding the thrust loss caused by Helix actuation). The actuation frequency was kept at an optimal value corresponding to $S_t = 0.28$. The incoming mean wind speed was set to $U_\infty = 8\,\mathrm{ms}^{-1}$.

Case	1	2	3	4	5	6	7	8	9	10	11
Helix Amplitude (°)	0	1	2	3	4	5	0	1	3	5	0
Turbulence Intensity (%)	2.0	2.0	2.0	2.0	2.0	2.0	4.0	4.0	4.0	4.0	8.2
Case	12	13	14	15	16	17	18	19	20	21	22
Helix Amplitude (°)	1	2	3	4	0	3	5	0	3	4	5
Turbulence Intensity (%)	8.2	8.2	8.2	8.2	10.3	10.3	10.3	13.1	13.1	13.1	13.1

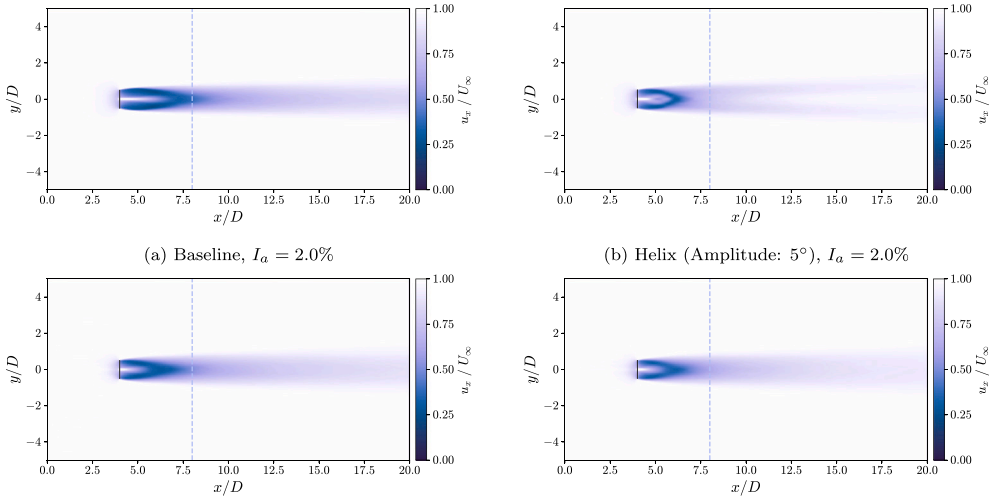

(a) Baseline, $I_a = 2.0\%$ (b) Helix (Amplitude: 5°), $I_a = 2.0\%$

(c) Baseline, $I_a = 13.1\%$ (d) Helix (Amplitude: 5°), $I_a = 13.1\%$

Fig. 2. Spatial and time-averaged streamwise velocity contours of the baseline cases (a, c) and maximally examined Helix actuation amplitude (b, d) for the lowest (top row), and highest turbulence case (bottom row). The dashed line indicates 4 D downstream of the turbine rotor.

the double-Gaussian distribution re-emerges. Notably, the rate at which these transformations occur is directly proportional to the applied actuation amplitude. Interestingly, for an actuation amplitude of 1°, this behavior was not observed. The velocity deficit transitions from the initial double-Gaussian into a single-Gaussian distribution without further changes in shape. However, its magnitude is still smaller than in the baseline case.

Fig. 3(b) demonstrates the dependence of time-averaged added TI profiles on the helical actuation amplitude. The added TI profiles were obtained by first calculating the total TI (TI_{tot}) for each point on the sampling plane as:

$$TI_{tot} = \frac{\sqrt{2k/3}}{\overline{U_\infty}}, \text{ where } k = \frac{1}{2}(u\prime^2 + v\prime^2 + w\prime^2), \tag{1}$$

where the $u\prime$, $v\prime$, and $w\prime$ are the fluctuations in x, y, and z directions respectively, and $\overline{U_\infty}$ is the streamwise mean wind speed.

The background TI (TI_{bg}) was then determined by averaging the TI values outside of the waked region. Lastly, its square was subtracted from the square of the total TI field, resulting in only the wake added TI (TI_{add}):

$$TI_{add} = \sqrt{TI_{tot}^2 - TI_{bg}^2}. \tag{2}$$

Consisten with observations in the velocity profiles, increased actuation amplitude accelerates the dissipation of the double-Gaussian distribution in the near-wake region. This leads to a pronounced increase in turbulence levels along the rotor plane centerline, particularly evident in the mid wake region. In the mid wake, the turbulence profile transitions into a bell-shaped distribution. For high actuation amplitudes, this characteristic shape is established as early as 3 D downstream, whereas the baseline case exhibits a much slower evolution towards this morphology, only materializing in the far wake. Furthermore, higher actuation amplitudes lead to an increase in the overall width of the turbulence profile. By 12 D downstream, the turbulence profiles for all actuation amplitudes converge and exhibit similarity to the baseline case.

Fig. 4 shows fits of the double-Gaussian (Eq. 4) to the velocity profiles obtained at different downstream distances. Key observations are that the fitted parameters of the double-Gaussian model are strongly influenced by the Helix actuation.

- **Lateral Gaussian Position (Fig. 4a):** The streamwise development of the lateral Gaussian peak separation $r_{\min}$ is directly proportional to the actuation amplitude. Higher amplitudes cause the function to reach its global minimum faster, while also causing a steeper rise of the function tail.
- **Gaussian Width (Fig. 4b):** The width (σ) of each Gaussian expands more rapidly in the near-wake with increasing actuation amplitude. Then, the linear growth in the tail becomes inversely proportional to the actuation amplitude.

3.2. Proposed velocity deficit formulation

The normalized velocity deficit $\Delta u(x,r)/u_{hub}$ at a downstream distance x and radial position r from the wake center is expressed using a double Gaussian shaping function to capture the transition from a

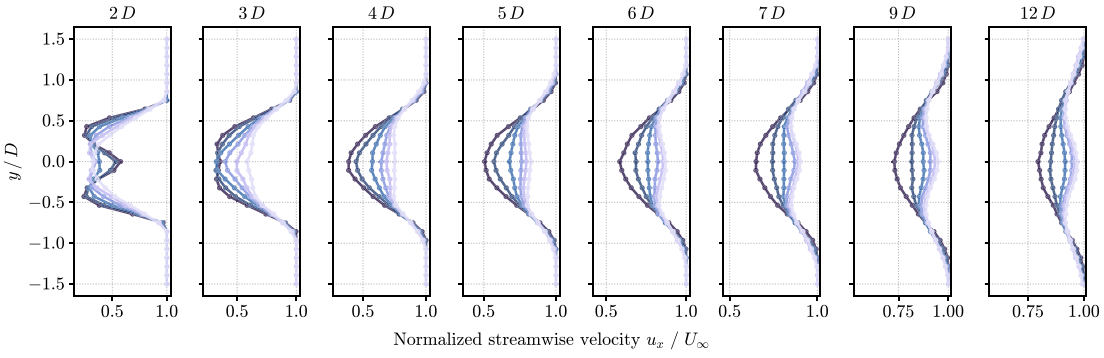

(a) Time-averaged velocity deficit profiles

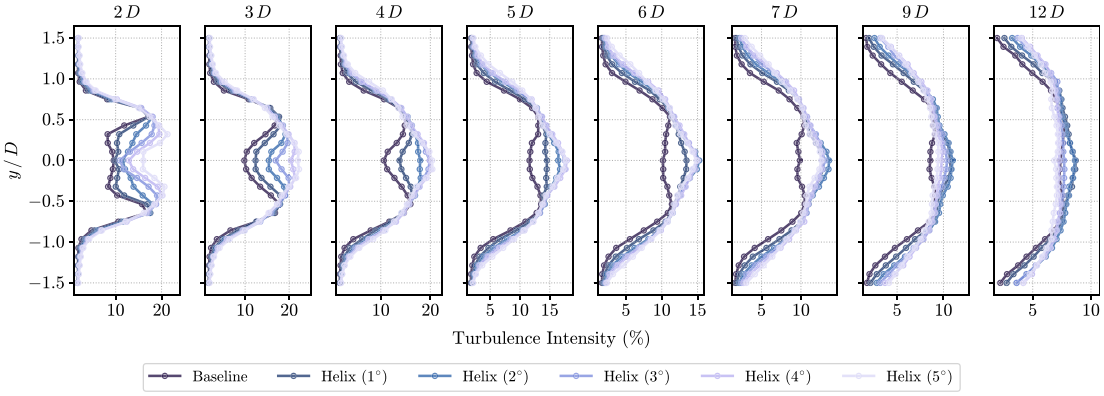

(b) Time-averaged added TI profiles

Fig. 3. Comparison of the downstream evolution of wake profiles for the baseline case and five cases with varying Helix actuation amplitudes (1°–5°) for an ambient TI of $I_a = 2.0\%$. (a) Shows the time-averaged streamwise velocity deficit profiles (u_x/U_∞ vs. y/D). The Helix actuation clearly accelerates wake recovery, as indicated by the reduction in the velocity deficit at all downstream locations compared to baseline operation. The magnitude of this effect is proportional to the actuation amplitude. (b) Time-averaged added TI profiles. The Helix cases generate significantly higher turbulence levels in the near-wake within the wake center.

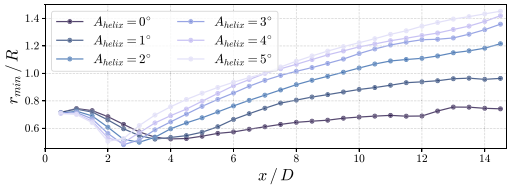

(a) Streamwise development of lateral gaussian position in crosswind distance normalized by the rotor radius R.

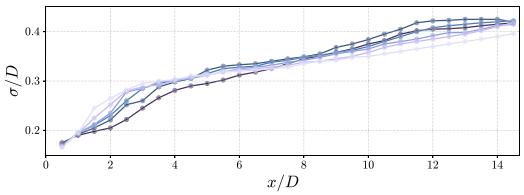

(b) Streamwise development of gaussian width normalized by the turbine diameter D

Fig. 4. Lateral Gaussian position (a) and Gaussian width (b), of the fitted standardized double-Gaussian (Eq. 4) for baseline and varying Helix actuation amplitudes.

near-wake double-peak profile to a flat-peak mid wake profile, to a far wake double-peak profile. The general form of the wake velocity deficit equation can be written as:

$$\frac{\Delta u(x,r)}{u_{hub}} = F(x)\phi(r), \tag{3}$$

where $F(x)$ denotes the amplitude function, and $\phi(r)$ the shaping function of the velocity deficit. The double Gaussian function, which is used here in its axisymmetric form, is defined as:

$$\phi(r) = \frac{1}{2}\left[\exp\left(-\frac{(r + r_{\min}(x))^2}{2\sigma(x)^2}\right) + \exp\left(-\frac{(r - r_{\min}(x))^2}{2\sigma(x)^2}\right)\right], \tag{4}$$

where $r_{\min}(x)$ denotes the radial position of the Gaussian peaks and $\sigma(x)$ the standard deviation (width) of the Gaussian peaks as a function of downstream distance. The model for the streamwise development of $r_{\min}$ is an extension of the non-linear Gaussian minimum function proposed by Qian and Ishihara [30]. A near-wake correction is incorporated to mitigate the unphysical high values the original function produces near the rotor plane when fitted to large Helix amplitudes.

$$\frac{r_{\min}}{R} = \begin{cases} f(0.6), & \text{if } \dfrac{x}{D} \le 0.6 \\ a\dfrac{x}{D} + b\left(1 + c\dfrac{x}{D}\right)^{-0.5} & \text{else,} \end{cases} \tag{5}$$

in which each unknown parameter ($a, b,$ and c) can be expressed through as a function (κ_{Helix}) of the thrust coefficient C_T, the ambient TI I_a, and the Helix amplitude A_{Helix}, extending the original original formula by Ishihara and Qian [44]:

$$\kappa_{r,Helix} = c_1 c_{T,h}^{c_2} I_a^{c_3} + \underbrace{\psi_1 A_{\text{Helix}}^{\psi_2} I_a^{\psi_3}}_{\text{Helix contribution}}, \tag{6}$$

with:

$$c_{T,h} = f(A_{\text{Helix}}), \tag{7}$$

where c_1, c_2, and c_3 are the baseline tuning parameters as proposed in the original formulation and ψ_1, ψ_2, and ψ_3 are the additional tuning parameters for the Helix wake.

The newly proposed formulation allows for additional tuning of the $r_{\min}$ function with respect to the actuation amplitude and incorporates the separate effect of ambient TI on the Helix wake while defaulting to the baseline parameterization for an actuation amplitude of 0°.

In the case of the function governing the streamwise development of σ, we propose to extend the original formulation in the following way:

$$\frac{\sigma}{D} = (1-\alpha)\left(k^*\frac{x}{D}+\varepsilon\right) + \alpha\gamma\ln\left(\frac{x}{D}+1\right)+\varepsilon, \tag{8}$$

with:

$$\alpha = \frac{A_{\text{Helix}}}{(A_{\text{Helix}}+\xi)}, \tag{9}$$

in which k^* and ε, expressed through their original formulation (κ) from [30], are the linear growth and y-offset of the baseline formulation, respectively. By introducing the blending factor α, the streamwise development for sigma defaults to the linear growth function in the case of baseline operation, while accounting for the steeper near-wake growth and flattening in the far wake in the case of increased Helix amplitudes. The new coefficients γ, ξ are expressed through:

$$\kappa_{\sigma,Helix} = \zeta_1 A_{\text{Helix}}^{\zeta 2} I_a^{\zeta_3}, \tag{10}$$

where ζ_1, ζ_2, and ζ_3 are the new tuning parameters for the Helix wake.

Note that σ represents the Gaussian standard deviation. For the overall double Gaussian wake boundary, the expression: $\pm(r_0 + 2\sqrt{2\ln 2\sigma})$, with $r_{1/2} = \sqrt{2\ln 2\sigma}$ representing the Gaussian half-width, is used.

For the amplitude function, $F(x)$, we adapt the third-order Taylor series expansion proposed by Qian and Ishihara [30]. This approach avoids the unphysical, complex values that the original formulation from Schreiber [29] produces for high thrust coefficients, while remaining consistent with momentum conservation. The original amplitude function and its Taylor series approximation are given by:

$$F(x) = \frac{M-\sqrt{M^2-1/2NC_TD^2}}{2N} \cong \frac{C_TD^2}{8M} + \frac{NC_T^2D^4}{64M^3} + \frac{N^2C_T^3D^6}{128M^5}, \tag{11}$$

where M and N are defined as:

$$M = 2\sigma^2 exp\left(-\frac{r_{\min}^2}{2\sigma^2}\right) + \sqrt{2\pi}r_{\min}\sigma\text{erf}\left(\frac{r_{\min}}{\sqrt{2}\sigma}\right), \tag{12}$$

$$N = \sigma^2\exp\left(-\frac{r_{\min}^2}{\sigma^2}\right) + \frac{\sqrt{\pi}}{2}r_{\min}\sigma\text{erf}\left(\frac{r_{\min}}{\sigma}\right), \tag{13}$$

with:

$$\text{erf}(x) = \frac{2}{\sqrt{\pi}}\int_0^x \exp(-t^2)dt. \tag{14}$$

3.3. Proposed added turbulence intensity formulation

To model wake-induced TI, we extend the well-known Frandsen approach [43] by incorporating the influence of a helical wake structure. This extension modifies both the magnitude and lateral spread of the added turbulence, making the model responsive to changes in actuation amplitude. While we acknowledge that this metric aggregates coherent vortex-induced fluctuations, it serves as an effective engineering descriptor for the downstream region that is critical to farm-level optimization.

The normalized radial offset from the wake centerline is given by:

$$d = \frac{\sqrt{(\Delta x)^2+(\Delta y)^2}}{D}, \tag{15}$$

where Δx and Δy are the streamwise and crosswind distances from the wake-emitting turbine. Based on this distance, the added TI at the center of the wake is defined as:

$$\text{TI}_{\text{add}} = \frac{1}{q_{f_H1} + q_{f_H2}\cdot\frac{d}{\sqrt{C_{t,h}}}}, \tag{16}$$

where q_{f_H1} and q_{f_H2} are empirical coefficients modelled as functions of the Helix amplitude A_{Helix}:

$$q_{f_H1} = f_1(A_{\text{Helix}}), \quad q_{f_H2} = f_2(A_{\text{Helix}}).$$

To account for lateral distribution of the wake turbulence, we adopt the angular bell-shaped weighting function proposed by Frandsen. The normalized downstream distance is given by:

$$s = \frac{\Delta x}{D}, \tag{17}$$

and the characteristic angular wake width is modified as:

$$\theta_w = \left(\frac{180}{\pi}\cdot\arctan\left(\frac{1}{s}\right)+10\right)\cdot\frac{1}{2}\cdot q_{f_H3}, \tag{18}$$

where $q_{f_H3} = f_3(A_{\text{Helix}})$ captures the Helix-induced spread of the turbulence profile. The actual angle between the affected point and the turbine centerline is computed by:

$$\theta = \begin{cases} \frac{180}{\pi}\cdot\arctan\left(\frac{\Delta y}{\Delta x}\right), & \text{if } \Delta x > 0 \\ 0, & \text{otherwise} \end{cases}. \tag{19}$$

The turbulence weight is then given by:

$$w = \begin{cases} \exp\left(-\left(\frac{\theta}{\theta_w}\right)^2\right), & \text{if } \theta < \theta_w \text{ and } \Delta x > 10^{-10} \\ 0, & \text{otherwise} \end{cases}. \tag{20}$$

Finally, the effective wake-added TI is computed as:

$$\text{TI}_{\text{eff}} = w\cdot\left(\sqrt{\text{TI}_{\text{add}}^2+\text{TI}_{\text{ambient}}^2} - \text{TI}_{\text{ambient}}\right), \tag{21}$$

where $\text{TI}_{\text{ambient}}$ is the ambient TI at the examined location. The square-root superposition follows the formulation proposed by Frandsen [43], while the Helix-based extension modifies both the maximum added turbulence and its lateral decay behavior.

The coefficient functions (q_{f_Hn}) can be expressed via quadratic fits in the form of:

$$q_{f_Hn} = p_1A_{\text{Helix}}^2 + p_2A_{\text{Helix}} + p_3 \tag{22}$$

in which the free parameters (p_n) can be obtained from experimental data or high-fidelity simulations.

4. Model calibration and validation

The models are validated by comparing their predictions of the velocity deficit and added turbulence profiles against the test dataset. First, the relationship between the Helix amplitude and the resulting thrust and power losses is established. To do this, the last 1800 s of turbine output data from each simulation was split into three pieces of 600 s each. Thrust and power measurements were time-averaged to obtain representative scalars and subsequently normalized by the corresponding baseline simulation values for each Helix amplitude. From these normalized quantities, the relative power and thrust losses were computed, providing the data shown in Fig. 5. A third-order polynomial model was then fitted to these data points, with the resulting coefficients listed in Table 2.

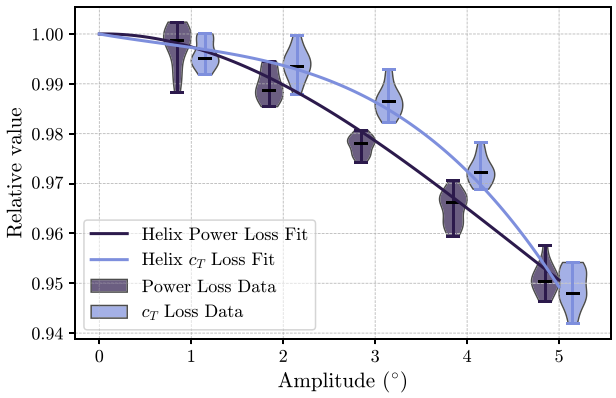

Fig. 5. Amplitude based thrust and power loss obtained from data points.

Table 2
Polynomial fit parameters for Helix loss functions. Each fit: $l_1\,A_{\text{Helix}}^3 + l_2\,A_{\text{Helix}}^2 + l_3\,A_{\text{Helix}} + l_4$.

Function	l_1	l_2	l_3	l_4
Helix power loss	2.30×10^{-4}	-3.20×10^{-3}	3.80×10^{-4}	1.00
Helix c_T loss	-4.70×10^{-4}	9.60×10^{-4}	-3.20×10^{-3}	1.00

4.1. Velocity deficit

The model parameters were calibrated using the training dataset. The calibration procedure focused on the wake region extending from the turbine rotor up to 12 D downstream. The objective was to minimize the Root-Mean-Square Error (RMSE) between the velocity fields predicted by the model, u_{model}, and those obtained from the LES, u_{LES}:

$$\text{RMSE} = \sqrt{\frac{1}{N}\sum_{i=1}^{N}(u_{\text{model},i} - u_{\text{LES},i})^2}, \tag{23}$$

where N is the total number of data points in the training set.

A two-stage optimization procedure was employed using the *scipy* library [45]. First, a global search was conducted using a differential evolution algorithm with the *best1bin* strategy (5000 generations, population size of 250) to broadly explore the parameter space. The solution was subsequently refined using the *L-BFGS-B* algorithm to find the local optimum.

The optimization process began with the baseline model coefficients and was followed by the tuning of the additional Helix parameters. The final calibrated values are presented in Table 3.

Fig. 6 illustrates the streamwise evolution of the Gaussian wake parameters, namely the radial position of the minimum velocity r_{min} and the wake width σ, for Helix actuation amplitudes A_{Helix} ranging from baseline operation (0°) to 5°. As shown in Fig. 6(a), the position of the deficit minimum r_{min} expands radially outward in direct proportion to the actuation amplitude. This behavior is consistent with the model's formulation, as discussed in Section 3. Similarly, Fig. 6(b) demonstrates that σ increases with larger actuation amplitudes in the near-wake, while transitioning to a more gradual growth in the far-wake, a characteristic governed by the implemented blending function.

The calibrated model is validated against the test dataset under different actuation amplitudes and ambient conditions. As a reference, the baseline prediction is shown. The results are presented in Fig. 7.

Fig. 7(a) demonstrates the model's ability to predict the wake evolution under various actuation amplitudes in low TI conditions. The proposed model accurately captures the transition of the wake profile from a single-Gaussian shape at low amplitudes to a distinct double-Gaussian distribution in the far wake at high amplitudes. Furthermore, the model's response to varying inflow conditions is highlighted in Fig. 7(b). It correctly predicts the reversion of a high-amplitude wake from a double- to a single-Gaussian profile as ambient turbulence increases.

As a result of its high fidelity in capturing these complex flow physics, the proposed model consistently achieves a low RMSE that is of the same order of magnitude as the baseline wake representation for all test cases across the entire downstream domain.

The proposed TI model demonstrates a high degree of accuracy when validated against the test dataset using the parameters from Table 4. As illustrated in Fig. 8, the model effectively captures the turbulence profile for various amplitudes, achieving an RMSE consistently below 2.5% for distances greater than 4 D from the rotor plane. Additionally, the RMSE for each Helix amplitude is lower than the baseline configuration between 3 and 9 D. The primary limitation occurs in the near-wake, where the model does not fully resolve the double-Gaussian turbulence structure, an issue more pronounced at lower actuation amplitudes. It should be noted that, to the best of our knowledge, this work presents the first low-fidelity model for Helix wakes including amplitude dependent TI, precluding a direct comparison with established alternatives.

Fig. 9 illustrates the normalized aerodynamic power (P_{wake}/P_∞) available to a virtual downstream turbine at distances ranging from $x/D = 2$ to 9. The proposed model is compared against the empirical Gaussian based active wake mixing model available in FLORIS [31], which was tuned on the same training data. The analysis considers the model's baseline configuration and two Helix actuation amplitudes of 3°

Table 3
Summary of parameter equations for r_{min} and σ functions.

Function/Model	Parameter	Equation
r_{min}	a	$= 0.085c_{T,h}^{0.57} I_a^{0.18} + 0.004A_{\text{Helix}}^{0.77} I_a^{-0.46}$
	b	$= 2.52c_{T,h}^{0.53} I_a^{0.001} - 0.044A_{\text{Helix}}^{0.14} I_a^{-0.036}$
	c	$= 34.4c_{T,h}^{1.25} I_a^{0.25} + 1.16A_{\text{Helix}}^{1.16} I_a^{-0.39}$
σ (Baseline)	k^*	$= 0.031c_{T,h}^{0.71} I_a^{0.01}$
	ε	$= 0.19c_{T,h}^{-0.018} I_a^{0.14}$
σ (Helix)	γ	$= 0.066A_{\text{Helix}}^{0.042} I_a^{-0.18}$
	ξ	$= 2.87A_{\text{Helix}}^{0.046} I_a^{-0.17}$

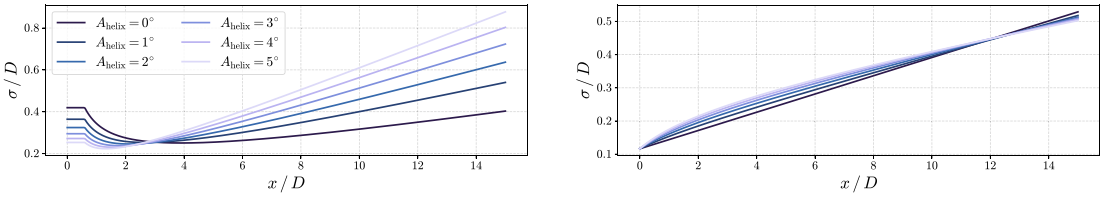

(a) Streamwise development of r_{min}/R.

(b) Streamwise development of σ/D.

Fig. 6. Evolution of (a) the minimum radius r_{min}/R and (b) the wake width σ/D with changing Helix amplitude for an ambient TI of $I_a = 2.0\%$.

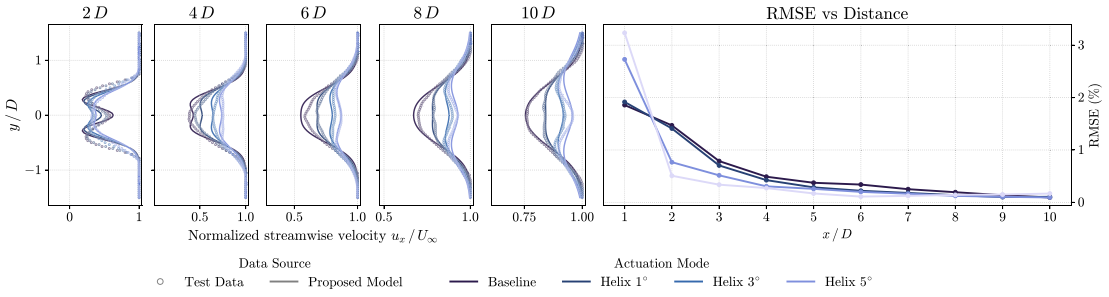

(a) Comparison for different Helix amplitudes with an ambient TI of $I_a = 2.0\%$.

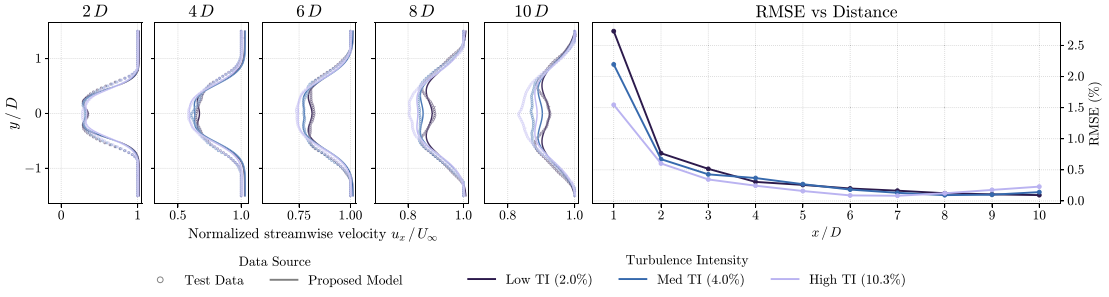

(b) Comparison for different TIs with an amplitude of 3°.

Fig. 7. Validation of the proposed velocity deficit model against the test dataset. Subfigure (a) shows the model's performance for varying Helix amplitudes (A_{Helix}) at a constant low TI. Subfigure (b) shows its performance for varying ambient TIs at a constant Helix amplitude.

Table 4
Quadratic fit parameters for q_{f_H1}, q_{f_H2}, and q_{f_H3} in the Helix turbulence model. Each fit: $p_1\, A_{\text{Helix}}^2 + p_2\, A_{\text{Helix}} + p_3$.

Function	p_1	p_2	p_3
q_{f_H1}	1.63×10^{-3}	-1.41×10^{-2}	4.29×10^{-2}
q_{f_H2}	-1.58×10^{-4}	1.42×10^{-3}	5.98×10^{-3}
q_{f_H3}	-2.93×10^{-3}	5.07×10^{-2}	1.11

and 5° under low ambient TI conditions. The aerodynamic power P_{wake} in the wake was calculated for a circular cross-section equivalent to the rotor area at various downstream distances as follows:

$$P_{wake,D_x} = \frac{1}{2}\rho \iint_A u(x, D_x)^3 \, dA, \tag{24}$$

with:

$$A = \pi\left(\frac{D}{2}\right)^2 \tag{25}$$

where $u(x, D_x)$ is the local velocity at position $x(r)$ at downstream distance D_x, and the air density is $\rho = 1.225$ kg.

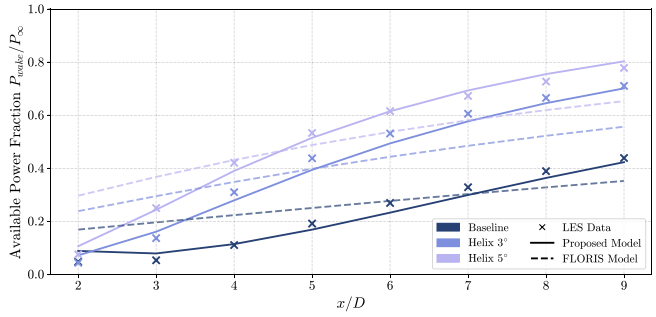

Fig. 9. Normalized aerodynamic power of a virtual turbine rotor at several downstream distances for the baseline configuration and the Helix amplitudes 3° and 5°.

The proposed engineering model (solid lines) shows excellent agreement with the high-fidelity LES data (markers) across all configurations. The proposed model accurately captures the non-linear recovery curvature that the FLORIS active wake mixing model (dashed lines) fails to predict. While the FLORIS model approximates the general trend, it exhibits significant deviations — particularly in the near-to-mid wake

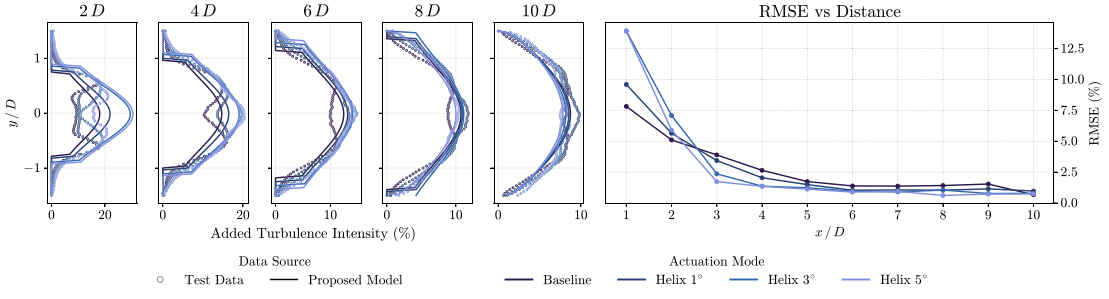

Fig. 8. Validation of the proposed wake added TI model against test data.

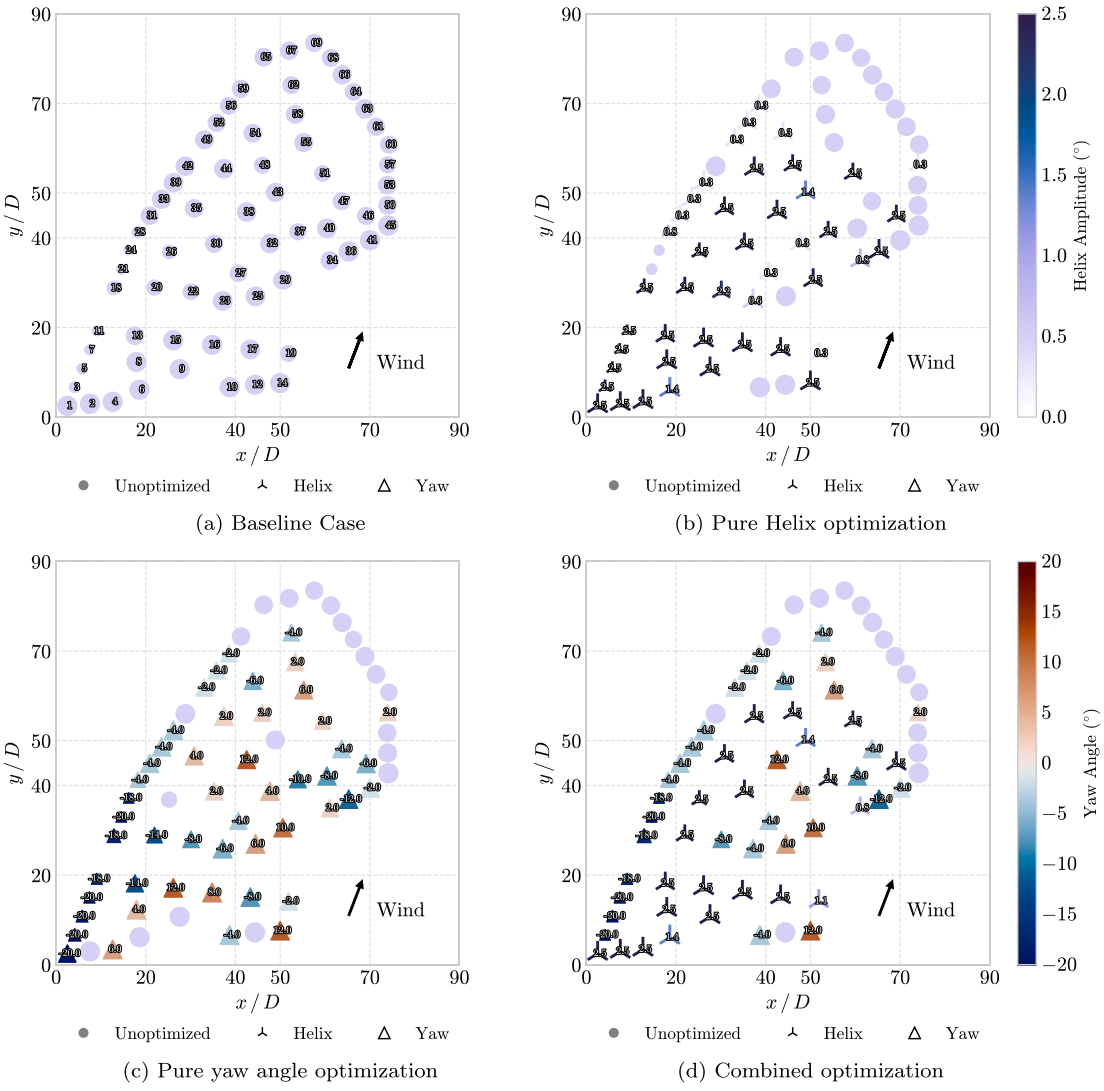

Fig. 10. Comparison of different control strategy settings for the scaled HKN wind farm with inflow conditions of wind direction 201°, wind speed of $U_\infty = 8\,\mathrm{ms}^{-1}$, and TI of $I_a = 4\%$. The size of each turbine marker is proportional to its power output. (a) Shows baseline operation without wake control in which the turbines are numbered according to their position relative to the incoming wind. (b) Optimization using only Helix control; turbine markers indicate Helix-controlled turbines, with the color and numbering corresponding to the Helix amplitude. (c) Optimization using only yaw control; triangles indicate yaw-controlled turbines, with the color and numbering corresponding to the yaw angle. (d) Combined optimization, where each turbine is individually optimized for either Helix or yaw control to maximize total farm power. The markers indicate whether wake steering or Helix control was chosen by the optimizer while the numbering indicates the magnitude of the respective chosen control strategy.

region ($x/D < 6$), whereas the proposed model consistently tracks the LES results with high precision.

5. Wind farm case study

The Hollandse Kust Noord (HKN) wind farm, located in the North Sea off the Dutch coast, was selected as the reference site for this study. It consists of 69 SG 11–200 turbines with a capacity of 11 MW each [46]. This site is representative of the next generation of large-scale offshore wind farms planned for the region. The turbine layout was derived from publicly available data [47] and scaled for a rotor diameter of $D = 284\,\mathrm{m}$. Within the open-source *PyWake* framework [48], the proposed models for velocity deficit and added TI were implemented as new wake and turbulence models, while the thrust and power loss functions from Section 4 were incorporated into a wind turbine model representing the IEA-22MW turbine. In addition, the *All2AllIterative* wind farm model class was modified to allow the Helix amplitude to be specified individually for each turbine while being able to account for blockage effects in the farm. All wake calculations within the *PyWake* environment were performed using the *LinearSum* superposition model together with the *Rathmann* blockage model, an analytical and computationally efficient approximation of the vortex cylinder solution derived in [49]. In the case of the turbulence superposition model, we chose the *SqrMaxSum* model. Velocity and turbulence at the rotor plane were sampled according to the circular Gauss integration, using 21 points [50]. This computational environment enabled the optimization of individual turbine control setpoints to maximize the total power output of the wind farm. For the Helix model, the actuation amplitudes were optimized up to an upper limit of 2.5°, in order to consider possible constraints on pitch bearings and actuators [16]. For a given wind direction, the turbines were sorted from upstream to downstream, and the actuation amplitude of each turbine n was varied from 0° to 2.5° in 0.1° increments to find the optimum farm power:

$$A_{Helix,opt,n}(u, I_a, \theta) = \underset{A_{Helix,n}}{\arg\max} \sum_{i=1}^{N} P_i(u, I_a, \theta), \tag{26}$$

Table 5
Comparison of mean total power output for each case and relative gain for the different control strategies under typical site conditions of $U_\infty = 8\,\mathrm{ms}^{-1}$ and $I_a = 4.0\%$.

Control strategy	Mean power (MW)	Mean gain (%)	Max gain (%)
Baseline	509.5	–	–
Only Helix	517.4	+1.6	+2.5
Only Wake Steering	523.1	+2.7	+6.1
Combined	527.4	+3.5	+7.1

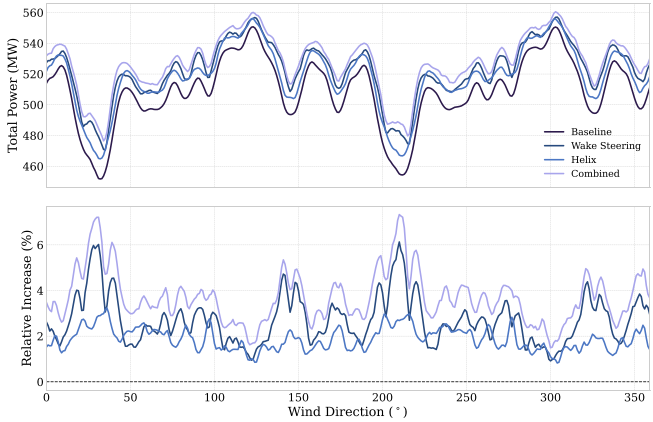

Fig. 11. Total power production per wind direction of each control strategy (top) and relative increase in baseline power production (bottom) for the reference wind farm (HKN) under typical ambient conditions $U_\infty = 8\,\mathrm{ms}^{-1}$ and ambient TI of $I_a = 4\%$.

where u is the wind speed at the rotor plane, I_a the TI at the rotor plane, and θ the wind direction. For benchmarking, the Helix strategy was compared against conventional wake steering, a more established wind farm control method that has been extensively studied, including in field tests [3,14,51]. The wake steering simulations were performed using the baseline calibration of the surrogate wake model in conjunction with the wake redirection model from [22]. The yaw angles for this case were optimized using a serial refine approach, closely following [52]. This process is repeated for each wind direction; it involves iterating through the turbines from upstream to downstream and selecting the yaw angle for each turbine from a discrete set of possible angles (−20° to 20° in 1° increments) that maximizes the cumulative farm power, formulated as:

$$\gamma_{opt,n}(u, I_a, \theta) = \arg\max_{\gamma_n} \sum_{i=1}^{N} P_i(u, I_a, \theta). \tag{27}$$

Finally, a combined optimization was performed in which each turbine could employ either Helix actuation or wake steering. For every wind direction, the turbines were again optimized in upstream-to-downstream order, with each turbine allowed to select either an actuation amplitude ($A_{Helix,n}$) or a yaw misalignment angle (γ_n) from their respective discrete sets. The chosen value was the one that maximized the overall wind farm power production:

$$S_{opt,n}(u, I_a, \theta) = \arg\max_{S_n \in A_{Helix,n}, \gamma_n} \sum_{i=1}^{N} P_i(u, I_a, \theta). \tag{28}$$

The results of this procedure for a representative inflow condition (201° wind direction, $8\,\mathrm{ms}^{-1}$ wind speed, and an ambient TI of I_a = 4%) are shown in Fig. 10. The figure compares baseline operation with pure Helix optimization, pure yaw optimization, and the combined strategy, illustrating how different control approaches influence turbine-level setpoints and the resulting power distribution across the farm. As shown, the combined strategy consistently achieves the highest total farm power, demonstrating the benefit of allowing turbines to flexibly choose between Helix actuation and yaw control.

When examining the farm-wide mean power production in Table 5, it becomes evident that combining the two approaches leads to highest possible power gain. This synergy can be attributed to the strengths of each method depending on the streamwise alignment of the turbine arrays: under direct alignment, Helix control outperforms wake steering, while under partial alignment, wake steering proves more effective, as demonstrated in previous studies [32,53].

This pattern is consistently observed across the entire wind rose, as shown in Fig. 11. In the combined case, each turbine is assigned the single control mode — either Helix or wake steering — that yields the highest local contribution to total farm power. By allowing this flexibility, the combined approach consistently outperforms the use of either strategy in isolation.

6. Conclusions

In this study, a novel steady-state engineering wake model for wind turbines under Helix actuation was developed, accounting for actuation amplitude and the specific impact of TI on the Helix wake. Based on observations from LES, the model extends the double-Gaussian formulation, originally proposed by Qian and Ishihara [30], to include Helix-specific coefficient formulations. Additionally, a model for wake-added TI was proposed by extending the bell-curve formulation, originally proposed by Frandsen [43], allowing for additional Helix amplitude-dependent parameterizations. Both models were tested against LES and showed high agreement with the test dataset across different operational and ambient conditions. Furthermore, the model was validated by evaluating the aerodynamic power within the wake for a virtual turbine rotor. This validation compared the baseline case against two Helix actuation amplitudes and the current industry-standard model (FLORIS active wake mixing model). The results demonstrated that the proposed model provides a significantly more accurate representation of power recovery in Helix-actuated wakes compared to existing steady-state tools.

Lastly, the models were integrated into the open-source *PyWake* framework to evaluate the effect of Helix control, both in comparison to and in coordination with wake steering on an upscaled version of an offshore wind farm. In our test case, we found that allowing turbines to select the most effective control mode — either Helix or wake steering — consistently outperforms using either approach in isolation, yielding farm-level power gains of over 7% under typical atmospheric conditions. Although the achieved gains depend on the ambient conditions, increases in power output were observed for all considered wind directions.

The availability of a more accurate engineering model for Helix-actuated wakes has significant implications for the design and operation of wind farms employing this control strategy. It can lead to more reliable predictions of power gains achievable with Helix control, facilitate improved optimization of Helix parameters for different ambient conditions, and allow for a more accurate assessment of potential changes in turbine loading patterns when integrated with a load surrogate model. These capabilities can contribute to better wind farm layout design, more effective control system development, and ultimately, a lower cost of wind energy.

CRediT authorship contribution statement

Tim Dammann: Writing – original draft, Visualization, Validation, Methodology, Investigation, Formal analysis, Data curation, Conceptualization. **Daan van der Hoek:** Writing – review & editing, Supervision, Software, Methodology, Investigation. **Wei Yu:** Writing – review & editing, Supervision, Methodology, Conceptualization. **Jan-Willem van Wingerden:** Writing – review & editing, Supervision.

Declaration of competing interest

The authors declare that they have no known competing financial interests or personal relationships that could have appeared to influence the work reported in this paper.

Acknowledgements

This work has been supported by the SUDOCO project, which receives the funding from the European Union's Horizon Europe Programme under the grant No. 101122256. The authors acknowledge the use of computational resources of the DelftBlue supercomputer, provided by Delft High Performance Computing Centre (https://www.tudelft.nl/dhpc). This work was carried out on the Dutch national e-infrastructure with the support of SURF Cooperative, using the Snellius supercomputer.

Data availability

Data will be made available on request.

References

[1] Crespo A, Hernández J, Frandsen S. Survey of wake models for wind turbine wakes. Wind Energy 1999;2(1):1–24. https://doi.org/10.1002/(SICI)1099-1824(199901/03)2:1<1::AID-WE14>3.0.CO;2-I
[2] Kheirabadi AC, Nagamune R. A quantitative review of wind farm control with the objective of wind farm power maximization. J Wind Eng Ind Aerodyn 2019;192:45–73.
[3] Howland MF, Lele SK, Dabiri JO. Wind farm power optimization through wake steering. Proc Natl Acad Sci 2019;116(29):14495–500.
[4] Meyers J, Bottasso C, Dykes K, Fleming P, Gebraad P, Giebel G, Gocmen T, van Wingerden JW. Wind farm flow control: prospects and challenges. Wind Energy Sci 2022;7(6):2271–306. https://doi.org/10.5194/wes-7-2271-2022
[5] Ciri U, Rotea MA, Leonardi S. Model-free control of wind farms: a comparative study between individual and coordinated extremum seeking. Renewable energy 2017;113:1033–45.
[6] Marden JR, Ruben SD, Pao LY. A model-free approach to wind farm control using game theoretic methods. IEEE Trans Control Syst Technol 2013;21(4):1207–14.
[7] Annoni J, Gebraad PM, Scholbrock AK, Fleming PA, Wingerden van J-W. Analysis of axial-induction-based wind plant control using an engineering and a high-order wind plant model. Wind Energy 2016;19(6):1135–50.
[8] Campagnolo F, Petrović V, Bottasso CL, Croce A. Wind tunnel testing of wake control strategies. In: 2016 American control conference (ACC). IEEE; 2016. p. 513–8.
[9] van der Hoek D, Kanev S, Allin J, Bieniek D, Mittelmeier N. Effects of axial induction control on wind farm energy production-a field test. Renew Energy 2019;140:994–1003.
[10] Bastankhah M, Porté-Agel F. Experimental and theoretical study of wind turbine wakes in yawed conditions. J Fluid Mech 2016;806:506–41.
[11] Howland MF, Bossuyt J, Martínez-Tossas LA, Meyers J, Meneveau C. Wake structure in actuator disk models of wind turbines in yaw under uniform inflow conditions. J Renew Sustain Energy 2016;8(4).
[12] Vollmer L, Steinfeld G, Heinemann D, Kühn M. Estimating the wake deflection downstream of a wind turbine in different atmospheric stabilities: an LES study. Wind Energy Sci 2016;1(2):129–41.
[13] Fleming P, Gebraad PM, Lee S, van Wingerden J-W, Johnson K, Churchfield M, Michalakes J, Spalart P, Moriarty P. Simulation comparison of wake mitigation control strategies for a two-turbine case. Wind Energy 2015;18(12):2135–43.
[14] Fleming P, Annoni J, Shah JJ, Wang L, Ananthan S, Zhang Z, Hutchings K, Wang P, Chen W, Chen L. Field test of wake steering at an offshore wind farm. Wind Energy Sci 2017;2(1):229–39.
[15] Munters W, Meyers J. Towards practical dynamic induction control of wind farms: analysis of optimally controlled wind-farm boundary layers and sinusoidal induction control of first-row turbines. Wind Energy Sci 2018;3(1):409–25.
[16] Frederik JA, Doekemeijer BM, Mulders SP, van Wingerden JW. The helix approach: using dynamic individual pitch control to enhance wake mixing in wind farms. Wind Energy 2020;23(8):1739–51.
[17] Korb H, Asmuth H, Ivanell S. The characteristics of helically deflected wind turbine wakes. J Fluid Mech 2023;965:A2. https://doi.org/10.1017/jfm.2023.390
[18] van der Hoek D, den Abbeele BV, Simao Ferreira C, van Wingerden JW. Maximizing wind farm power output with the helix approach: experimental validation and wake analysis using tomographic particle image velocimetry. Wind Energy 2024. https://doi.org/10.1002/WE.2896
[19] van Vondelen AA, Navalkar ST, Kerssemakers DR, van Wingerden JW. Enhanced wake mixing in wind farms using the helix approach: a loads sensitivity study. In: 2023 American control conference (ACC). IEEE; 2023. p. 831–6.
[20] Taschner E, van Vondelen A, Verzijlbergh R, van Wingerden JW. On the performance of the Helix wind farm control approach in the conventionally neutral atmospheric boundary layer. J Phys Conf Ser 2023;2505(1):012006. https://doi.org/10.1088/1742-6596/2505/1/012006. https://dx.doi.org/10.1088/1742-6596/2505/1/012006.
[21] Frederik JA, van den Broek M, van Wingerden JW. Synchronized helix: a feedback control approach to phase-synchronized wake steering. Wind Energy 2024;27(4):e3223. https://doi.org/10.1002/we.3223
[22] Jiménez Á, Crespo A, Migoya E. Application of a LES technique to characterize the wake deflection of a wind turbine in yaw. Wind Energy 2010;13(6):559–72.
[23] Larsen GC, Ott S, Liew J, van der Laan MP, Simon E, Thorsen GR, Jacobs P. Yaw induced wake deflection-a full-scale validation study. In: Journal of physics: conference series, vol. 1618. IOP Publishing; 2020, p. 062047.
[24] Jensen NO. A note on wind generator interaction. Risø National Laboratory; 1983.
[25] Frandsen S, Barthelmie R, Pryor S, Rathmann O, Larsen S, Højstrup J, Thøgersen M. Analytical modelling of wind speed deficit in large offshore wind farms. Wind Energy Int J Prog Appl Wind Power Convers Technol 2006;9(1–2):39–53.
[26] Bastankhah M, Porté-Agel F. A new analytical model for wind-turbine wakes. Renew Energy 2014;70:116–23.
[27] Keane A, Aguirre PEO, Ferchland H, Clive P, Gallacher D. An analytical model for a full wind turbine wake. In: Journal of physics: conference series, vol. 753. IOP Publishing; 2016, p. 032039.
[28] Keane A. Advancement of an analytical double-gaussian full wind turbine wake model. Renewable Energy 2021;171:687–708.
[29] Schreiber J, Balbaa A, Bottasso CL. Brief communication: a double-gaussian wake model. Wind Energy Sci 2020;5(1):237–44.
[30] Qian G-W, Ishihara T. A novel double-gaussian full wake model for wind turbines considering dependence on thrust coefficient and ambient turbulence intensity. Appl Energy 2025;391:125859.
[31] NREL. Floris: A controls-oriented engineering wake model. version 4.1.1, BSD-3-Clause License, 2024, https://github.com/nrel/floris.
[32] Dammann T, van der Hoek D, Yu W, van Wingerden JW. Enhanced wind farm performance via active wake control: a steady-state approach. In: 2025 American control conference (ACC). IEEE; 2025. p. 2856–61.
[33] Exawind. Amr-wind: adaptive mesh refinement for wind. 2023, https://github.com/Exawind/amr-wind [accessed: 23 January 2025].
[34] Zhang W, et al. Amrex: a framework for block-structured adaptive mesh refinement. J Open Source Softw 2019;4(37):1370. https://doi.org/10.21105/joss.01370
[35] Sharma A, et al. ExaWind: open-source CFD for hybrid-RANS/LES geometry-resolved wind turbine simulations in atmospheric flows. Wind Energy 2024;27(3):225–57. https://doi.org/10.1002/we.2886.
[36] Borges R, Carmona M, Costa B, Don WS. An improved weighted essentially non-oscillatory scheme for hyperbolic conservation laws. J Comput Phys 2008;227(6):3191–211. https://doi.org/10.1016/J.JCP.2007.11.038
[37] Jonkman J. The new modularization framework for the fast wind turbine CAE tool; Jan 2013). https://doi.org/10.2514/6.2013-202. https://www.osti.gov/biblio/1068607.
[38] Zahle F, et al. Definition of the IEA wind 22-megawatt offshore reference wind turbine. Tech. Rep. DTU Wind Report E-0243, Technical University of Denmark, International Energy Agency; 2024. https://doi.org/10.11581/DTU.00000317
[39] Kelley ND, Jonkman BJ. Overview of the Turbsim stochastic inflow turbulence simulator: version 1.21 (revised February 1, 2001). Apr, 2007. https://doi.org/10.2172/903073.
[40] Dammann T, Dangi N, van Wingerden JW, Yu W. Benchmark study on rotor performance, wake dynamics, and atmospheric boundary layers using NREL Sowfa-6 and Amr-Wind. In: Journal of physics: conference series, vol. 3016. IOP Publishing; 2025, p. 012034.
[41] NREL. ROSCO. Version 2.4.1. 2021, https://github.com/NREL/ROSCO.
[42] van der Hoek D, den Abbeele BV, Simao Ferreira C, van Wingerden J-W. Maximizing wind farm power output with the helix approach: experimental validation and wake analysis using tomographic particle image velocimetry. Wind Energy 2024;27(5):463–82. https://doi.org/10.1002/we.2896.
[43] Frandsen S. Turbulence and turbulence-generated structural loading in wind turbine clusters [Ph.D. thesis, risø-R-1188 (EN)]. 2007.
[44] Ishihara T, Qian G-W. A new gaussian-based analytical wake model for wind turbines considering ambient turbulence intensities and thrust coefficient effects. J Wind Eng Ind Aerodyn 2018;177:275–92.
[45] Virtanen P, et al. SciPy 1.0: fundamental algorithms for scientific computing in Python. Nature Methods 2020;17:261–72. https://doi.org/10.1038/s41592-019-0686-2
[46] Crosswind. Hollandse Kust Zuid wind farm sites i-IV. 2025, https://www.crosswindhkn.nl/windfarm/ [accessed: 17 September 2025].
[47] 4C Offshore. Global offshore renewable map. 2024, https://map.4coffshore.com/offshorewind/ [accessed: 25 September 2024].
[48] M. M. P. Pywake 2.5.0: an open-source wind farm simulation tool. Feb, 2023. et al. https://gitlab.windenergy.dtu.dk/TOPFARM/PyWake.
[49] Branlard E, Gaunaa M. Cylindrical vortex wake model: right cylinder. Wind Energy 2015;18(11):1973–87.
[50] Abramowitz M, Stegun IA. Handbook of mathematical functions: with formulas, graphs, and mathematical tables, vol. 55. Courier Corporation; 1965.
[51] Simley E, Fleming P, Girard N, Alloin L, Godefroy E, Duc T. Results from a wake-steering experiment at a commercial wind plant: investigating the wind speed dependence of wake-steering performance. Wind Energy Sci 2021;6(6):1427–53.
[52] Fleming PA, Stanley APJ, Bay CJ, King J, Simley E, Doekemeijer BM, Mudafort R. Serial-refine method for fast wake-steering yaw optimization. In: Journal of Physics: conference series, vol. 2265. IOP Publishing; 2022, p. 032109.
[53] Taschner E, Becker M, Verzijlbergh R, van Wingerden JW. Comparison of helix and wake steering control for varying turbine spacing and wind direction. Journal Phys Conf Ser 2024;2767(3):032023. https://doi.org/10.1088/1742-6596/2767/3/032023.